Journal of The Electrochemical Society, 2022 **169** 100512
1945-7111/2022/169(10)/100512/6/$40.00 © 2022 The Electrochemical Society ("ECS"). Published on behalf of ECS by IOP Publishing Limited

Spatiotemporal Visualization and Chemical Identification of the Metal Diffusion Layer at the Electrochemical Interface

Yuxin Zhang,[1,=] Anyang Hu,[1,=] Evan Maxey,[2] Luxi Li,[2,z] and Feng Lin[1,z]

[1]*Department of Chemistry, Virginia Tech, Blacksburg, VA 24073, United States of America*
[2]*Advanced Photon Source, Argonne National Laboratory, Lemont, IL 60439, United States of America*

The diffusion layer created by transition metal (TM) dissolution is ubiquitous at the electrochemical solid-liquid interface and plays a key role in determining electrochemical performance. Tracking the spatiotemporal dynamics of the diffusion layer has remained an unresolved challenge. With spatially resolved synchrotron X-ray fluorescence microscopy and micro-X-ray absorption spectroscopy, we demonstrate the in situ visualization and chemical identification of the dynamic diffusion layer near the electrode surface under electrochemical operating conditions. Our method allows for direct mapping of the reactive electrochemical interface and provides insights into engineering the diffusion layer for improving electrochemical performance.
 [DOI: 10.1149/1945-7111/ac964b]

Manuscript submitted July 8, 2022; revised manuscript received September 7, 2022. Published October 10, 2022.

Supplementary material for this article is available online

Transition metal (TM) dissolution in liquid environments is a common degradation mechanism in corrosion and electrochemical energy systems.[1–5] The reactive solid-liquid interface experiences dynamic dissolution processes and exhibits various reformation behaviors, such as surface phase segregation,[6] selective incorporation of foreign ions,[7] and morphological evolution.[8–10] Driven by the concentration gradient and electric field, the dissolved TM species can form a diffusion layer in the solid-liquid region.[11] Such a diffusion layer can modulate the interfacial mass transfer and influence the chemical and electrochemical behaviors of bulk materials.[12–15] Therefore, understanding the formation and evolution of the diffusion layer is valuable for quantifying interfacial processes and guiding materials design.

To date, identifying the dynamic processes at the solid-liquid interface has remained a key challenge, especially when spatiotemporal resolution is needed. To the best of our knowledge, most experimental efforts have failed to track the population and chemical properties of dissolved species near the electrode surface. The widely adopted ex-situ characterizations, such as inductively coupled plasma mass spectrometry, can accurately measure the concentration of dissolved species while typically losing the capability of real-time probing at the interface.[3,16,17] In comparison, some in situ techniques, such as interferometric microscopy,[18] UV–Vis,[19] and dye-assisted laser scanning confocal microscopy,[20] are suitable for probing the dynamic evolution of diffusion layers. However, these approaches lack either spatial resolution or elemental sensitivity. Hence, a suitable experimental design is in urgent need to better understand how the diffusion layer evolves and how the dissolved TM species transform under different conditions.

Given the complexity of the solid-liquid interface, the experimental method desires to fulfill the following requirements: (1) simultaneous detection of multiple elements with high sensitivity, favorably in the sub-ppm range; (2) sufficient spatial resolution; (3) capability of in situ measurements under operating conditions; (4) chemical and structural characterization of lattice and dissolved TM species, including oxidation states and local chemical environments; (5) large-area scanning (μm to mm) to ensure statistical representativeness.

Herein, we combine X-ray fluorescence microscopy (XFM) and micro-X-ray absorption near-edge spectroscopy (μ-XANES) to investigate the spatiotemporal evolution of the TM diffusion layer under electrochemical conditions. The new approach is demonstrated with $LiMn_2O_4$ (LMO) for Li^+ electrochemistry and WO_3 for H^+ electrochemistry in aqueous electrolytes. We reveal the dynamic evolution of the diffusion layer and compare the varying TM electronic structures across the electrochemical interface. Our new approach demonstrates great potential to spatially visualize and quantify the diffusion layer evolution at reactive electrochemical interfaces.

We design a three-electrode in situ cell (Fig. 1a) to conduct interfacial studies with XFM and μ-XANES under operating conditions. We mount the in situ cell to the cell holder with the incident X-ray perpendicular to the reaction chamber (Fig. 1b). To initiate the X-ray fluorescence phenomena, the incident X-ray energy should exceed the excitation/binding energy of the element of interest and in this work, Mn K (6.539 keV) and W L_3 (10.207 keV).

The incident X-ray is attenuated by the aqueous electrolyte, while a small portion of X-ray photons are absorbed by TM species and generate X-ray fluorescence signals. These fluorescent X-ray photons can be absorbed by the sample itself while propagating to the detector, in a process known as self-absorption, which is stronger for low-Z elements because low-energy photons are less penetrating. Figure 1c shows the X-ray transmission as a function of water thickness and photon energy. If the penetration depth (or escape depth for fluorescent X-rays) is defined as X-ray propagation distance when the transmission reduces to 1/e, the Mn Kα emission (5.899 keV) should have an escape depth of ~400 μm and W Lα1 emission (8.398 keV) would have an escape depth of ~1,200 μm.

LMO is a widely studied Li-ion battery cathode material for aqueous batteries owing to its excellent bulk stability and relatively high energy density.[21–24] The Mn dissolution induced by the aggravated Jahn-Teller distortion in the presence of protons is an important degradation mechanism for LMO cathodes.[12] Meanwhile, the dissolved Mn species can be redeposited onto the electrode surface, forming electrochemically inactive deposits and deteriorating battery performance. Here, we choose LMO as a platform to investigate the buildup and dynamics of the diffusion layer formed by Mn cations in the aqueous electrolyte (2 M LiTFSI).

To better identify the formation of the diffusion layer, we first measure the morphology of the top surface and cross-section of the dry LMO sample (Supplemental Figs. 1 and 2), which shows the heterogeneous nature of the pristine electrode. As shown in Fig. 2a, clear image contrast can be observed, which can be attributed to the sharp change in the Mn concentration across the solid-air interface. We extract the vertical line profile that summarizes the counts of each pixel to quantitatively estimate the intensity drop. Figure 2b displays ten line profiles processed from the yellow-shaded area in Fig. 2a. Ideally, if a sample is horizontally placed, the trendline of intensity drop should be perpendicular to the background baseline where the intensity is equal to 0. However, the zoomed-in region of the averaged curve for ten line profiles, shown in Fig. 2c, exhibits a

[=]Equal Contribution.
[z]E-mail: luxili@anl.gov; fenglin@vt.edu

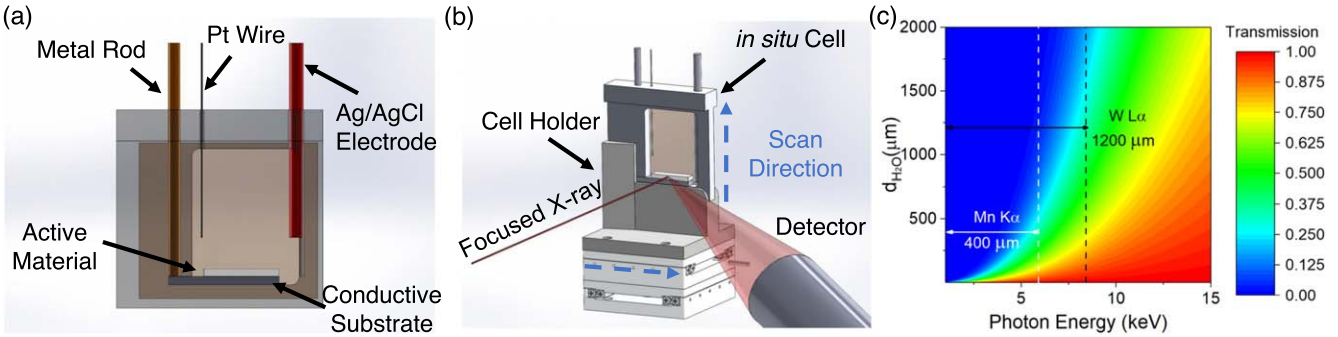

Figure 1. (a) The zoom-in image of the in situ cell, which can accommodate three electrodes. The metal rod is isolated from the aqueous electrolyte with sole contact with the conductive substrate, where the active material is attached to. The cell is sealed with Kapton tape and epoxy to avoid electrolyte leakage; (b) The scheme of the experimental setup at the beamline 2 ID-D of Advanced Photon Source. The in situ cell is placed into the cell holder and fixed on the sample stage. The electrolyte thickness along the beam direction is 5 mm. A silicon-drift energy-dispersive detector is located ∼30° from the X-ray propagation direction to collect the fluorescent X-ray photons. Under the raster scan mode, the sample stage moves horizontally and vertically to allow for continuous data acquisition over a large area. (c) The fluorescence transmission is a function of photon energies and water thickness, where the emission energies for Mn Kα1 and W Lα1 are labeled with white and black dashed lines, respectively. The corresponding probing depths are labeled in the figure.

tilted trendline, suggesting a slight incline of the sample. The deviation is determined to be ∼7 μm by measuring the distance between intersection point A and zero-intensity point B. This value is consistent with the value obtained from the average line profile of the entire image (∼6 μm calculated from 50 line profiles), which confirms that the selected area is representative for further studies (Supplemental Figs. 3a and 3b).

After injecting the aqueous electrolyte (2 M LiTFSI) into the cell, the pixel intensity in the solid phase exhibits three orders of magnitude decay due to the strong water absorption (Fig. 2e). Since the XFM image presented here is a 2D projection, the intensity for the dry electrode reflects accumulated Mn concentration within the entire sample along the X-ray beam direction. In contrast, the intensity for the electrode soaked in the electrolyte only originates from the regions of the electrode that are shallowly submerged along the X-ray beam direction. Therefore, owing to the non-uniform LMO distribution intrinsic to the drop-casted sample, the spatial intensity of the electrode soaked in the electrolyte (Fig. 2d) becomes more heterogeneous compared to the dry electrode (Fig. 2a). In contrast to the sharp intensity drop at the solid-air interface, we can observe a sloping solid-to-liquid transition in Fig. 2f, demonstrating the buildup of the Mn diffusion layer in the aqueous electrolyte and validating the feasibility of this method to map metal diffusion layers. Considering the shallow penetration depth of X-ray in the electrolyte and the negligible tilting of samples, the thickness of the Mn diffusion layer is estimated to be ∼32 μm. (Fig. 2f and Supplemental Figs. 3c and 3d).

In comparison, after the cell is electrochemically cycled within −0.1–1.5 V (vs Ag/AgCl) using the cyclic voltammetry (CV) technique at 5 mV s^{-1} for one cycle (Supplemental Fig. 4), the overall intensity is further decreased (Figs. 2g and 2h), implying continuous Mn dissolution under the electrochemical polarization. The movement of particles during electrochemical cycling is possible, thus we analyze the average line profiles of the shaded area (Fig. 2g) and the entire probed region (Supplemental Figs. 3e and 3f) to improve statistical representativeness and avoid the inaccurate information caused by the particle movement. Figure 2i and Supplemental Figs. 3e–3f show that the diffusion layer greatly diminishes after the CV measurement, which is likely due to the electrolytic water decomposition at high voltage. The gas bubbles generated from the oxygen evolution reaction (OER) can perturb the diffusion layer.

We also investigate the evolution of the diffusion layer under constant charging/discharging conditions and the corresponding voltage profile is shown in Supplemental Fig. 5. The thickness of the diffusion layer is identified to be ∼38 μm when the pristine electrode is soaked in the electrolytes (Figs. 3a–3c), which agrees with the above results (Fig. 2f). When the LMO electrode is fully charged to 1.2 V vs Ag/AgCl without triggering OER, the Mn dissolution can be observed (Fig. 3d) and the thickness of the diffusion layer is extended to ∼47 μm (Figs. 3e–3f). The propagation of the diffusion layer can originate from two aspects: (1) the charging-induced Mn dissolution increases the Mn concentration in the interfacial region and promotes the dissolved Mn species to diffuse further; (2) the electric field provides a driving force for a longer traveling distance of dissolved Mn species. The thickness of the diffusion layer remains unchanged at the fully discharged state (Figs. 3g–3i), indicating that an equilibrium has been established for the Mn diffusion layer. Overall, with different electrochemical protocols applied to the LMO electrode, we demonstrate a new method that enables the direct visualization of the buildup and dynamic evolution of the diffusion layer in the aqueous electrolyte.

Beyond measuring the dynamics of the TM diffusion layer, identifying the chemical properties of dissolved TM species is also important. Herein we show that our set-up can also be applied to investigate the oxidation states and chemical environments of dissolved species through μ-XANES. Hence, the WO_3 material with higher absorption energy of W (Lα: ∼10□2 keV) is selected as our platform. The morphology of WO_3 is shown in Supplemental Fig. 6. When the sample is immersed in 0.5 M H_2SO_4 electrolyte and held at −0.1 V (vs Ag/AgCl), a fixed X-ray beam energy (10.25 keV) is first utilized to probe the formation of the W diffusion layer. Due to the high intensity of the fluorescence signals (Fig. 4a), the line profile (Fig. 4b) is illustrated on the log scale to highlight the variation of local counts. Using the same approach we described earlier, the thickness of the W diffusion layer is estimated to be 19 μm (Fig. 4b and Supplemental Fig. 7). The smaller W diffusion layer thickness compared to that of LMO can be potentially ascribed to the much thinner WO_3 film (∼1 μm) and lower W solubility and diffusion coefficient. A wider range of potential conditions (−0.165 V and 0.635 V) have been used to study the evolution of the diffusion layer, which shows a negligible variation (Supplemental Fig. 8). The electron excitation from W $2p_{3/2}$ to W 5d unoccupied states gives rise to the prominent resonance of μ-XANES (Fig. 4e).[25] The strongest absorption peak is also known as the white line (WL). The W L_3-edge μ-XANES spectrum collected at the D0 position is identical to the signal from the WO_3 bulk electrode without electrolyte, validating the feasibility of our μ-XANES probing across the interface (Supplemental Fig. 9). The peak position of the WL remains constant from D0 to D20 (Fig. 4e), indicating a constant W oxidation state (i.e., W^{6+}) throughout the diffusion layer.[26] The shape of the WL can infer the local symmetry. We have not observed the splitting feature of the WL of the W L_3-edge spectra (from the D0 to D20, Figs. 4d–4e), denoting that our local W units are neither dihedral (D_2) nor ideal octahedral (O_h) symmetry.[27] The WL with only one peak usually indicates distorted octahedral

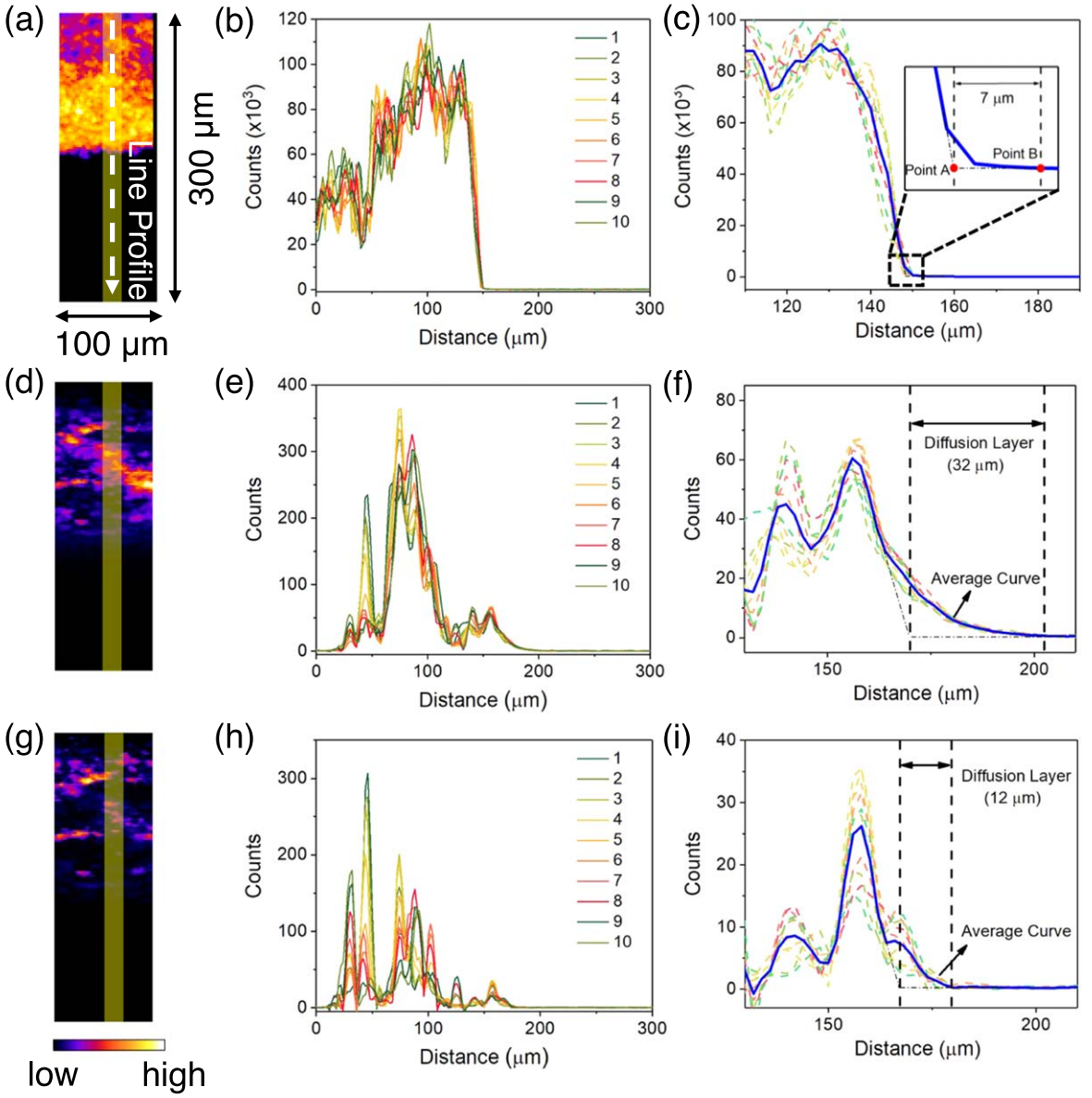

Figure 2. (a) The XFM image of the LMO electrode at the solid-air interface without adding the electrolyte; (b) The line profiles calculated from the yellow-shaded region in (a), exhibiting a sharp intensity drop during the solid-to-air transition; (c) The zoomed-in region of the averaged curve derived from ten line profiles in (b), which implies an intrinsic deviation of ~7 μm caused by the tilting of the working electrode, and corresponding to a tilted angle of ~0.1° (estimated by arctan(7 μm/5 mm), where the 5 mm is the width of the sample; (d) the XFM image of LMO sample after injecting the 2 M LiTFSI electrolyte and (g) after one complete cyclic voltammetry cycle between −0.1 and 1.5 V vs Ag/AgCl (Supplemental Fig. 4). The line profiles of the shaded area are shown in (e) and (h), and the corresponding averaged curves are shown in (f) and (i), demonstrating the formation and dynamics of the diffusion layer. The dashed arrow in (a) indicates the scanning direction of the presented line profiles. The image dimension is 300 μm × 100 μm and the size of each pixel is 2 × 2 μm^2.

structures.[27] Here, the W L_3-edge spectrum at the D0 position has a sharp WL peak, while the one at the D20 position has a broad WL peak, indicating a higher degree of distortion.[27] Therefore, our results show that the W local environment transforms from the solid WO_3 electrode to the dissolved W species at the interface while the W oxidation state remains unchanged. If the absorption spectra can be measured with an extensive energy range at the post-edge region, it would also provide information on the exact chemical environment surrounding W. In summary, by combining in situ XFM and μ-XANES techniques under electrochemical conditions, we demonstrate that our method can not only measure the dynamics of TM dissolution but also identify the chemical properties of dissolved species.

Applying the technique to non-aqueous electrolyte systems is feasible after a careful screening of the properties of organic solvents (e.g., boiling point, vapor pressure) to satisfy safety needs. Moreover, to obtain an accurate result, the electrode surface should be flat and exhibit negligible change upon electrochemical cycling, as reflected in Figs. S10 and S11 for both LMO and WO_3 electrodes. Last but not least, a proper selection of the scan area, step size, and dwell time of the measurements can balance the spatial and temporal resolution and yield high-quality data.

To conclude, combining in situ XFM and μ-XANES techniques, we directly track TM dissolution behavior at electrochemical interfaces with a good spatiotemporal resolution. For the first time, we can simultaneously investigate the dynamic formation and evolution of the TM diffusion layer and study the oxidation state and local coordination environment of dissolved species at the interface. This method opens up new opportunities for in situ detection of ion diffusion dynamics under concentration and electrical field gradients. Further expansion of the method could also include more X-ray techniques, such as X-ray diffraction and

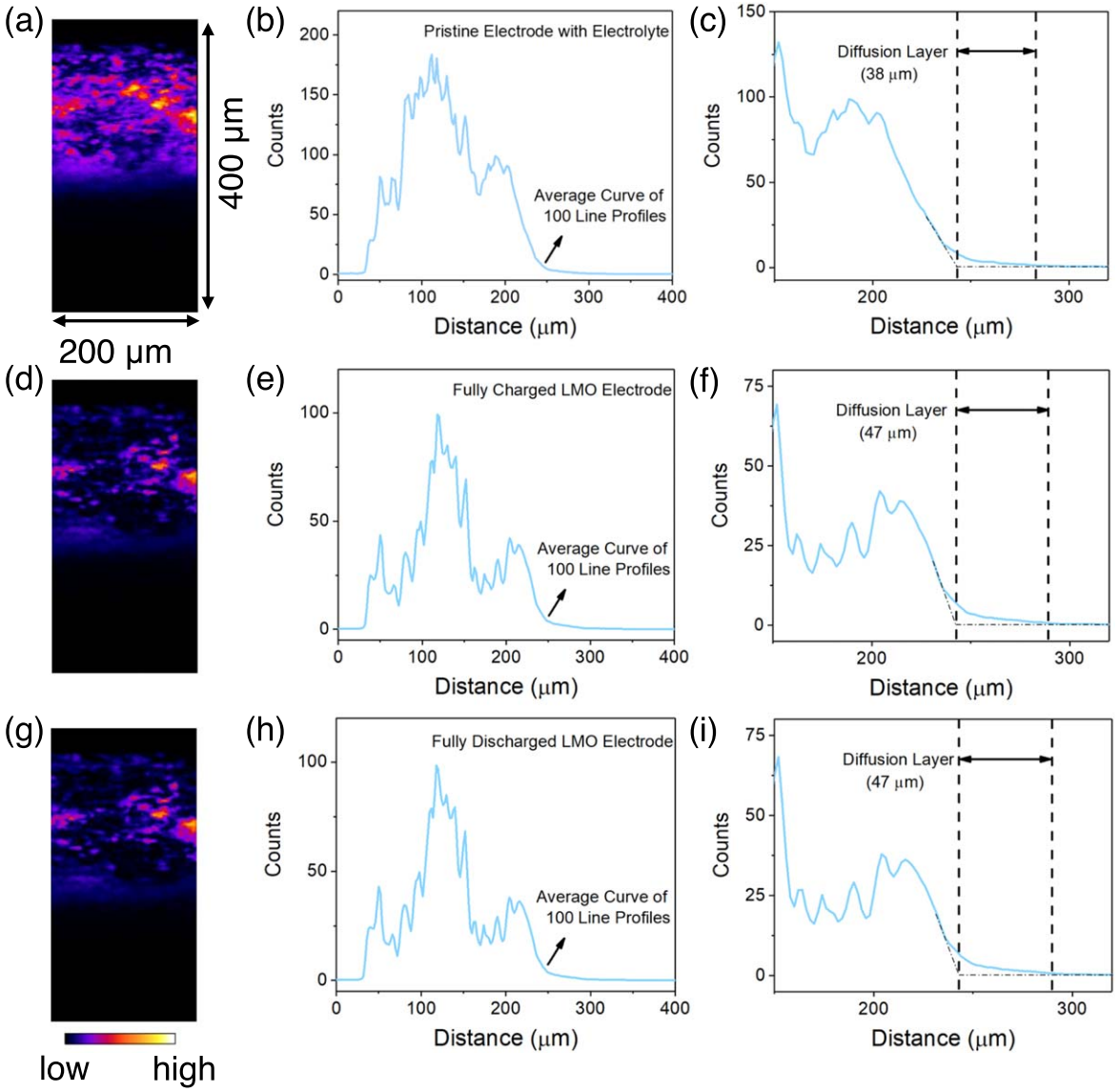

Figure 3. The evolution of diffusion layer under constant current charging/discharging conditions. (a) The XFM image of the pristine LMO electrode soaked in the electrolyte; (b) The averaged line profile derived from 100 line profiles in (a); (c) The zoomed-in region of the line profile, showing a diffusion layer thickness of ~38 μm. The XFM image of LMO samples at (d) fully charged state (1.2 V vs Ag/AgCl) and (g) fully discharged state (0 V vs Ag/AgCl). The averaged line profiles are shown in (e) and (h), and the corresponding thickness of the diffusion layer is shown in (f) and (i). The image dimension is 400 μm × 200 μm and the size of each pixel is 2 × 2 μm^2.

scattering to track the phase evolution and agglomeration of nanoparticles at the solid-liquid interface and to reveal the size and shape of the reactive complexes under operating conditions.

Experimental

Material preparation.—The $LiMn_2O_4$ (LMO) was provided by the U.S. Department of Energy's (DOE) CAMP Facility (Cell Analysis, Modeling and Prototyping) at Argonne National Laboratory. The WO_3 thin films on fluorine-doped tin oxide (FTO) glass substrate (MSE Supplies) were prepared using spraying deposition and low-temperature calcination methods. The specific procedure can be found in our previous report.[8] The thickness of the deposited WO_3 thin film was ~1 μm. The width of the substrate was cut to 5 mm to fit the customized reaction cell.

Electrochemical measurement.—In the three-electrode system, Ag/AgCl (3M NaCl) (MF-2052, BASi Research) and Pt wire (Sigma Aldrich) were utilized as reference and counter electrodes, respectively. The $LiMn_2O_4$ (LMO) slurry was prepared by mixing active materials, carbon black and polyvinylidene fluoride (PVDF) with a ratio of 8:1:1 and then drop-casted onto carbon paper. The electrode thickness is estimated to be ~90 μm. The mass loading was estimated to be ~5 mg cm^{-2}. The electrolyte was prepared by dissolving 2 M Lithium bis(trifluoromethanesulfonyl)imide (LiTFSI) in DI water. The cyclic voltammetry (CV) measurement was applied to the LMO electrode at a scan rate of 5 mV s^{-1} within −0.1–1.5 V (vs Ag/AgCl). The constant charging-discharging measurement was conducted in the in situ cell. The voltage range was 0–1.2 V (vs Ag/AgCl) and the current density was 20 mA g^{-1}. For the electrochemical measurements of WO_3 samples, 0.5 M H_2SO_4 was used as the electrolyte. The chronoamperometry (CA) test was performed on the WO_3 samples with the potential holding at −0.1 V (vs Ag/AgCl) for 60 min. All electrochemical measurements were conducted using the Potentiostat (SP-150, BioLogic, France).

In situ XFM measurement.—The drop-casted LMO electrodes with 0.5 × 2 cm^2 size were attached to the conductive substrate using epoxy. Both LMO and WO_3 samples were inserted into the

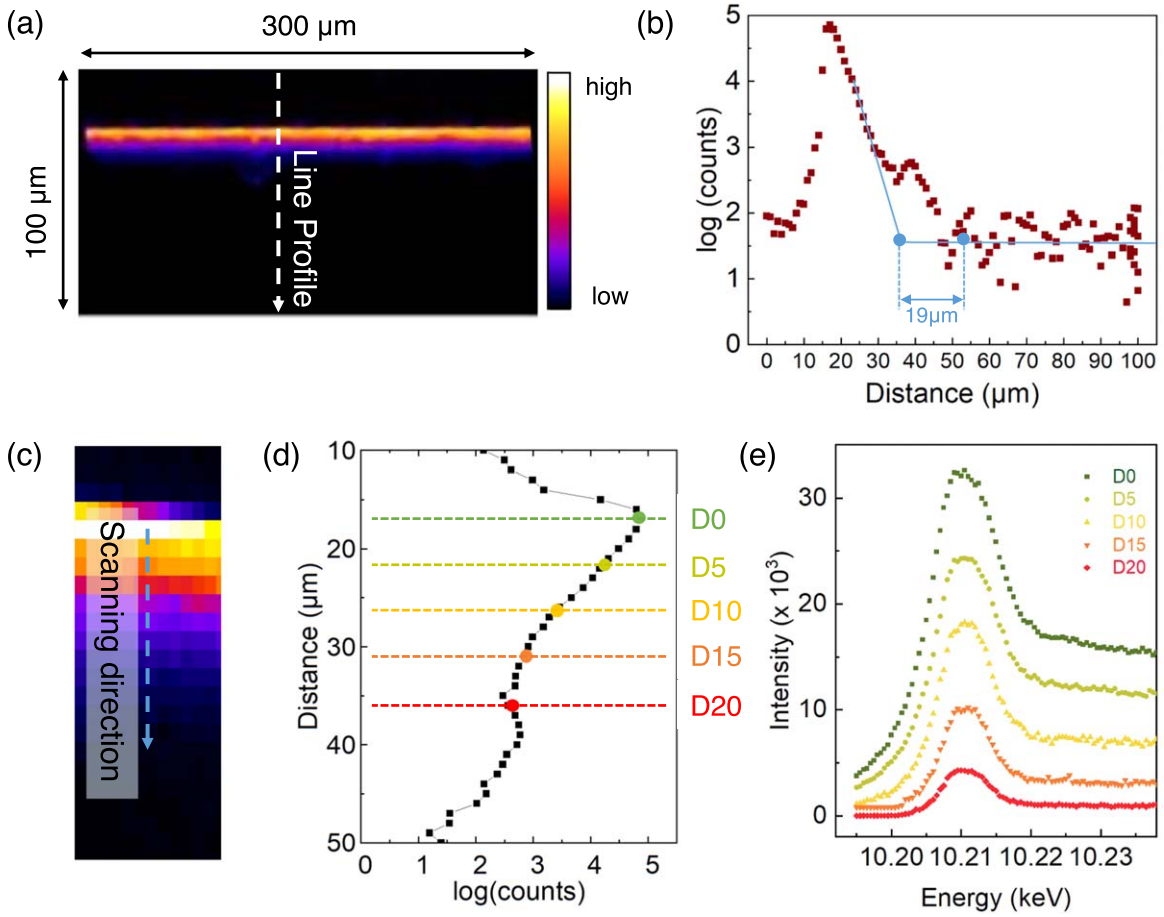

Figure 4. (a) Representative XFM image of spray-calcined WO_3 film on a fluorine-doped tin oxide (FTO) substrate and immersed in a 0.5 M sulfuric acid (H_2SO_4) electrolyte. The image dimension is 300 μm × 100 μm and the size of each pixel is 1 × 1 μm^2. (b) With the XFM line profile, log (counts) is a function of the distance shown in (a). The auxiliary lines (in blue) are drawn to estimate the thickness of the diffusion layer in the WO_3-H_2SO_4 electrochemical cell. (c) The enlarged XFM image highlights the X-ray scanning direction during the collection of μ-XANES data. (d) The corresponding μ-XANES data collection positions, where D0 represents the brightest starting point, and D5 to D20 represent the subsequent μ-XANES data collection positions, with an interval of 5 μm. (e) Experimental μ-XANES spectra at the W L_3-edge. The spectra are collected when the potential of the WO_3 electrode is held at −0.1 V vs Ag/AgCl. The white arrow in (a) indicates the direction of the presented line profile.

cell, after which the cell was sealed with Kapton tape and epoxy. Then electrolytes were injected into the cell. The in situ XFM was performed at the 2-ID-D beamline of Advanced Photon Source, Argonne National Laboratory. The X-rays generated by the synchrotron radiation were selected by a Si(111) double-crystal monochromator at 10.25 keV and focused by a Fresnel zone plate onto the sample with a spot size of 300 nm. The solid/electrolyte interface is raster-scanned over a large area with coarse resolution. The step sizes for LMO and WO_3 samples were 2 μm and 1 μm, respectively. The fluorescent X-ray signals were detected with a single element silicon-drift Vortex detector and the raw data were processed and quantified with MAPS.

***In situ* μ-*XANES measurement.*—**Micro-X-ray absorption near-edge spectroscopy (μ-XANES) at the W L_3-edge was performed in the fluorescence mode at the Advanced Photon Source Beamline 2-ID-D. The X-ray energy was scanned from 10.195 keV to 10.250 keV with a 0.5 eV step. Solid WO_3 electrodes and dissolved W species in the liquid electrolyte were identified by their μ-XANES signals. Within D0, D5, D10, D15, and D20 five positions, different dwell times were used to ensure an adequate signal-to-noise ratio of the white line of each μ-XANES spectrum. The total time needed for acquiring μ-XANES at five positions sequentially was around 44 min. All μ-XANES spectra were energy calibrated using the white line position of a W metal foil and normalized with the Athena software.

Acknowledgments

The work was supported by the National Science Foundation under no. CBET 1912885. This research used resources of the Advanced Photon Source, a U.S. Department of Energy (DOE) Office of Science User Facility operated for the DOE Office of Science by Argonne National Laboratory under Contract no. DE-AC02-06CH11357. We thank Dr. Cheng-Jun Sun for the W L_3-edge hard X-ray absorption spectroscopy measurement of bulk WO_3 electrode without electrolyte at the beamline 20-BM-B at the Advanced Photon Source, Argonne National Laboratory.

Author contribution

Y.Z. and A. H. contributed to the work equally. F.L. conceived and led the project. Y.Z., A.H., L.L., and F.L. designed experiments and participated in manuscript preparation. Y.Z. and A.H. performed material synthesis, XFM measurements, and data analysis. E.M. participated in the discussion and figure preparation. All authors approved the final draft of the manuscript.

ORCID

Yuxin Zhang https://orcid.org/0000-0002-2830-4159

References

1. T. Bellezze, G. Giuliani, A. Viceré, and G. Roventi, *Corros. Sci.*, **130**, 12 (2018).

2. W. B. Hawley, A. Parejiya, Y. Bai, H. M. Meyer III, D. L. Wood III, and J. Li, *J. Power Sources*, **466**, 228315 (2020).
3. T. Liu, A. Dai, J. Lu, Y. Yuan, Y. Xiao, L. Yu, M. Li, J. Gim, L. Ma, and J. Liu, *Nat. Commun.*, **10**, 4721 (2019).
4. S. Maiti, R. Konar, H. Sclar, J. Grinblat, M. Talianker, M. Tkachev, X. Wu, A. Kondrakov, G. D. Nessim, and D. Aurbach, *ACS Energy Lett.*, **7**, 1383 (2022).
5. J. Guo, J. Ming, Y. Lei, W. Zhang, C. Xia, Y. Cui, and H. N. Alshareef, *ACS Energy Lett.*, **4**, 2776 (2019).
6. C. Kuai, Z. Xu, C. Xi, A. Hu, Z. Yang, Y. Zhang, C.-J. Sun, L. Li, D. Sokaras, and C. Dong, *Nat. Catal.*, **3**, 743 (2020).
7. C. Kuai, C. Xi, A. Hu, Y. Zhang, Z. Xu, D. Nordlund, C.-J. Sun, C. A. Cadigan, R. M. Richards, and L. Li, *J. Am. Chem. Soc.*, **143**, 18519 (2021).
8. A. Hu, Z. Jiang, C. Kuai, S. McGuigan, D. Nordlund, Y. Liu, and F. Lin, *J. Mater. Chem. A*, **8**, 20000 (2020).
9. H. Yang, X. Chen, N. Yao, N. Piao, Z. Wang, K. He, H.-M. Cheng, and F. Li, *ACS Energy Lett.*, **6**, 1413 (2021).
10. Y. Zhang, C. Kuai, A. Hu, L. Ma, S. Tan, I. Hwang, L. Mu, M. M. Rahman, C.-J. Sun, and L. Li, *ACS Appl. Mater. Interfaces*, **14**, 12130 (2022).
11. A. D. McNaught and A. Wilkinson, *Compendium of Chemical Terminology* (Blackwell Science, Oxford) 1669 (1997).
12. C. Zhan, T. Wu, J. Lu, and K. Amine, *Energy Environ. Sci.*, **11**, 243 (2018).
13. A. Sood, A. D. Poletayev, D. A. Cogswell, P. M. Csernica, J. T. Mefford, D. Fraggedakis, M. F. Toney, A. M. Lindenberg, M. Z. Bazant, and W. C. Chueh, *Nat. Rev. Mater.*, **6**, 847 (2021).
14. J. A. Gilbert, I. A. Shkrob, and D. P. Abraham, *J. Electrochem. Soc.*, **164**, A389 (2017).
15. A. Molina, J. González, E. Laborda, and R. G. Compton, *Phys. Chem. Chem. Phys.*, **15**, 2381 (2013).
16. D. Huang, C. Engtrakul, S. Nanayakkara, D. W. Mulder, S.-D. Han, M. Zhou, H. Luo, and R. C. Tenent, *ACS Appl. Mater. Interfaces*, **13**, 11930 (2021).
17. Y. Jin, Y. Xu, P. M. L. Le, T. D. Vo, Q. Zhou, X. Qi, M. H. Engelhard, B. E. Matthews, H. Jia, and Z. Nie, *ACS Energy Lett.*, **5**, 3212 (2020).
18. A. Miki, K. Nishikawa, G. Kamesui, H. Matsushima, M. Ueda, and M. Rosso, *J. Mater. Chem. A*, **9**, 14700 (2021).
19. G. Zhou, X. Sun, Q.-H. Li, X. Wang, J.-N. Zhang, W. Yang, X. Yu, R. Xiao, and H. Li, *J. Phys. Chem. Lett.*, **11**, 3051 (2020).
20. B. Fuladpanjeh-Hojaghan, M. M. Elsutohy, V. Kabanov, B. Heyne, M. Trifkovic, and E. P. L. Roberts, *Angew. Chemie*, **131**, 16971 (2019).
21. L. Suo, O. Borodin, T. Gao, M. Olguin, J. Ho, X. Fan, C. Luo, C. Wang, and K. Xu, *Science*, **350**, 938 (2015).
22. P. Jaumaux, X. Yang, B. Zhang, J. Safaei, X. Tang, D. Zhou, C. Wang, and G. Wang, *Angew. Chemie Int. Ed.*, **60**, 19965 (2021).
23. J. Xie, Z. Liang, and Y.-C. Lu, *Nat. Mater.*, **19**, 1006 (2020).
24. D. Dong, J. Xie, Z. Liang, and Y.-C. Lu, *ACS Energy Lett.*, **7**, 123 (2021).
25. Y. Ren, Y. Zou, Y. Liu, X. Zhou, J. Ma, D. Zhao, G. Wei, Y. Ai, S. Xi, and Y. Deng, *Nat. Mater.*, **19**, 203 (2020).
26. U. Jayarathne, P. Chandrasekaran, A. F. Greene, J. T. Mague, S. DeBeer, K. M. Lancaster, S. Sproules, and J. P. Donahue, *Inorg. Chem.*, **53**, 8230 (2014).
27. S. Yamazoe, Y. Hitomi, T. Shishido, and T. Tanaka, *J. Phys. Chem. C*, **112**, 6869 (2008).